Rare Metal Materials and Engineering
Volume 51, Issue 8, August 2022
Available online at www.rmme.ac.cn

Science Press

Cite this article as: Li Yuyu, Han Tingzhuang, Chu Zhibing, et al. Effect of Strain Path on Mechanical Behavior of AZ31 Magnesium Alloy[J]. Rare Metal Materials and Engineering, 2022, 51(08): 2785-2793.

ARTICLE

Effect of Strain Path on Mechanical Behavior of AZ31 Magnesium Alloy

Li Yuyu[1], Han Tingzhuang[2], Chu Zhibing[1], Xue Chun[1], Yang Qianhua[1], Zhao Xiaodong[1], Gao Hong[3]

[1] College of Materials Science and Engineering, Taiyuan University of Science and Technology, Taiyuan 030024, China; [2] School of Materials Science and Engineering, Northwestern Polytechnical University, Xi'an 710072, China; [3] Jiangsu Wujin Stainless Steel Co., Ltd, Changzhou 213000, China

Abstract: Extruded AZ31 magnesium alloy was used as raw specimens, and pre-deformation experiments were conducted in the direction of ∥ED (extrusion direction) and ⊥ED at room temperature. The instantaneous deformation stress state of a cross-sectional reduced wall was simulated in the cold Pilgering process. Then, the pre-deformed specimens were sampled for secondary compression, and the microstructure after two deformations was characterized by electron backscatter diffraction. The effects of structure and texture on mechanical behavior under the condition of strain path change were investigated. Results show that the yield strength of the AZ31 magnesium alloy is improved by pre-deformation. The improvement is attributed to the $\{10\bar{1}2\}$ tension twins resulting from the pre-deformation, further resulting in grain refinement and increase in dislocation density. Moreover, the appearance of twinning changes the grain orientation. The weakening of the basal texture (or the strengthening of the twin texture) may play an important role in improving the mechanical properties of the AZ31 magnesium alloy. The yield strength of the ∥ED-3% and ⊥ED-3% samples is increased by 66.7% and 6.6%, respectively.

Key words: AZ31 magnesium alloy; strain path; mechanical behavior; twin; dislocation; texture

Magnesium and its alloys are lightweight structural materials whose density is approximately 30% lower than that of aluminum alloy and a quarter of that of steel. As structural materials, magnesium alloys have attracted extensive attention in the automotive and aerospace fields[1-5]. However, the critical resolved shear stress (CRSS) ratio of the non-basal slip to the basal slip of a wrought magnesium alloy at room temperature is large, and the independent slip system at room temperature is limited; these conditions lead to the poor formability of the wrought magnesium alloy, which seriously restricts its development[6-8].

The deformation behavior of metal materials during single loading is substantially different from that during multiple loading. The strain path dependence of a single loading has been well studied for magnesium alloys. Park et al[9] studied the tension-compression asymmetry of a randomly textured cast magnesium alloy according to its $\{10\bar{1}2\}$ twinning characteristics. Wang et al[10] used electron backscatter diffraction (EBSD) to investigate the twinning activity of the AZ31 magnesium alloy under uniaxial compression at room temperature. Su et al[11] studied the effect of initial texture of the AZ31 magnesium alloy on its $\{10\bar{1}2\}$ twinning variant selection mechanism. However, with respect to practical engineering applications, the deformation mechanism of the magnesium alloy under a multi-directional stress state and a complex strain path is rarely studied. Hou et al[12] integrated $\{10\bar{1}2\}$ tension twins into an AZ31 magnesium alloy sheet during compression deformation at room temperature along the TD direction and found that the material's yield strength and ultimate strength increase significantly during secondary compression along the RD direction. Song et al[13] found that pre-deformation can introduce dislocations and produce a

Received date: August 27, 2021
Foundation item: National Key R&D Program of China (2018YFB1307902); National Natural Science Foundation of China (U1710113); Joint Postgraduate Training Base of Shanxi Province (2018JD33); Shanxi Excellent Youth Fund (201901D211312); Transformation and Cultivation Project of Scientific and Technological Achievements in Colleges and Universities of Shanxi Province (2019KJ028); Postgraduate Education Innovation Program of Shanxi Province (2019SY482)
Corresponding author: Chu Zhibing, Ph. D., Professor, College of Materials Science and Engineering, Taiyuan University of Science and Technology, Taiyuan 030024, P. R. China, Tel: 0086-351-2776763, E-mail: chuzhibing@tyust.edu.cn

Copyright © 2022, Northwest Institute for Nonferrous Metal Research. Published by Science Press. All rights reserved.

large number of tension twins. On the one hand, the existence of twins can make the crystal rotate and change grain's textural strength and type. On the other hand, the interaction of twins can refine the grain. Wang et al[14] found that the compression-extrusion process greatly influences grain refinement and textural weakening and effectively improves the tension/compression asymmetry of extruded magnesium alloy rods without sacrificing their strength. Some studies show that a tube is in a multi-directional stress state and can form under the complex strain path during cold Pilgering[15,16]. Moreover, the textural characteristics after deformation can greatly influence the succeeding deformation process. Therefore, the textural evolution characteristics and deformation mechanism of a sample in this region need to be analyzed.

In this study, on the basis of the analysis of the cold pilgering process, the AZ31 magnesium alloy bar was cut into cubes and pre-deformed at room temperature along //ED (extusion direction) and ⊥ED to simulate the instantaneous deformation stress state of the cross-sectional reduced wall (i. e., "two compressions and one tension"). Then, the pre-deformed specimens were sampled for secondary compression. The mechanical behavior of the AZ31 magnesium alloy in different strain paths was analyzed by EBSD to reveal the deformation mechanism of tube formation. The findings can provide a theoretical basis for tube formation and expand the application of magnesium alloy tubes.

1 Experiment

1.1 Pre-deformation

Fig. 1a shows a cold Pilgering model that is mainly composed of a top roll, a bottom roll, a tube, and a mandrel. The process action explored in this study follows the characteristics of the presented model. The mandrel keeps motion under the restriction of a chuck, and the top and bottom rolls can move back and forth. The tube forms by continuous quantitative feeding and quantitative rotation. Fig. 1b presents a schematic diagram of the stress characteristic location in the instantaneous deformation of the cross section of a tube in the reduced wall section. Region I is selected for stress analysis. The circumferential stress σ_θ and radial stress σ_r represent compressive stress, whereas the axial stress σ_l represents tension stress.

A physical simulation experiment was performed on the tube deformation in the reduced wall section based on the abovementioned analysis. The mold shown in Fig. 2 has been designed for physical simulation at room temperature. The die was composed of the punch, die, adjusting gasket, wedge block 1, wedge block 2, and pre-deformation sample. The sample was placed in the die for pre-deformation and subjected to two-way compression and one-way tension. The adjusting gasket was designed to control the amount of pre-deformation.

Fig. 3 shows the stress distribution of the pre-deformed sample, which can be roughly divided into three regions. The

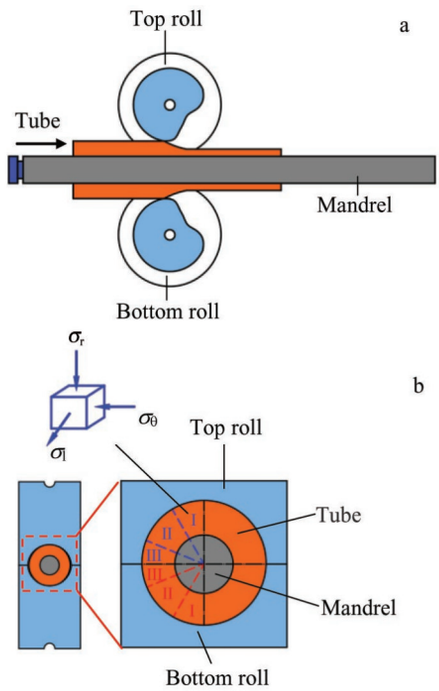

Fig.1 Illustration of the tube cold Pilgering process and section stress analysis: (a) cold Pilgering model; (b) stress characteristic location in the instantaneous deformation of the cross section of a tube in the reduced wall section

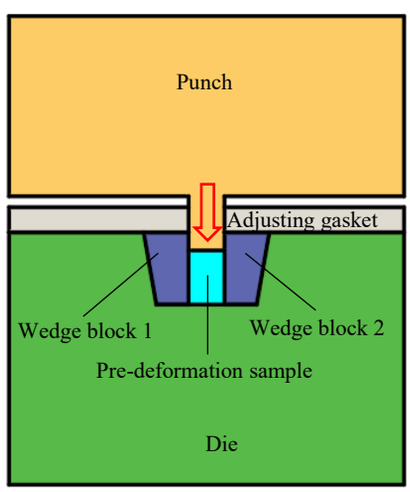

Fig.2 Overall assembly drawing of mold

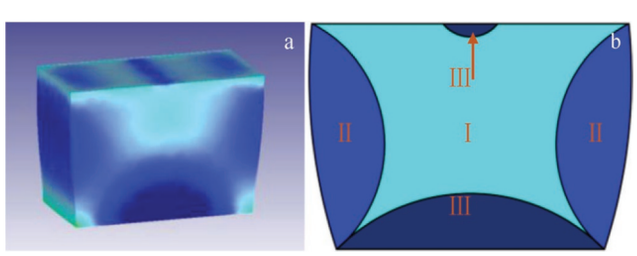

Fig.3 Distribution of stress structure of pre-deformed sample: (a) simulation diagram and (b) simplified schematic

stress of region I is the largest, followed by region II, whereas region III is hardly deformed. The corresponding regions are called large deformation region (I), free deformation region (II), and difficult-to-deformation region (III).

The raw material used in this study was a commercially extruded AZ31 magnesium alloy with a diameter of 40 mm. As shown in Fig. 4, the pre-deformation sample (20 mm×27 mm×30 mm) was obtained by wire cutting. Two kinds of pre-deformation experiments at a constant strain rate of 10^{-3} s^{-1} were carried out on the electrical servo motor testing machine (model: WAW-1000) provided by Changchun Kexin Test Instrument Co., Ltd in Jilin Province of China at room temperature. The experiments for the loading axis that was positioned parallel and perpendicular to the extrusion direction (ED) were called ⊥ED and //ED, respectively. The surface characterized by EBSD before and after deformation was explored on the ED×TD side.

Fig. 5 shows the IPF diagram, grain boundary misorientation, and {0002} and $\{10\bar{1}0\}$ pole figures on a longitudinal section extruded bar before deformation. The EBSD technique is used for the measurement. The initial structure of the extruded bar is mainly composed of equiaxial grains (Fig. 5a). The base plane of most grains of the initial sample is almost parallel to the ED direction, and the $\{10\bar{1}0\}$ plane of most grains is perpendicular to the ED direction. The textural strength of the base surface can reach 11.18. The small-angle (2°~15°) grain boundary accounts for 9%, whereas the large-angle (>15°) grain boundary accounts for 91%.

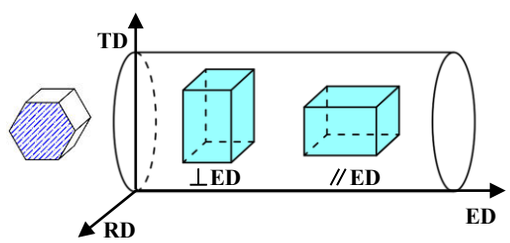

Fig.4 Sampling method of the pre-deformation sample

1.2 Secondary compression

The large deformation area (I) of the pre-deformed sample is shown in Fig. 6a. The 3% pre-deformed samples are numbered as //ED-3% and ⊥ED-3%. For comparison, the samples without pre-deformation are numbered as //ED-0% and ⊥ED-0%, and the compression sample is 6 mm×8 mm×12 mm cuboid, as shown in Fig. 6b. The secondary compression experiments were carried out by the electronic universal testing machine (model: WDW-E100D) provided by Changchun Kexin Test Instrument Co., Ltd in Jilin Province of China at room temperature. The loading direction was 12 mm, and the selected strain rate was 10^{-3} s^{-1}.

2 Results and Discussion

2.1 Pre-deformation

Fig. 7, which includes the IPF diagram, grain boundary structure diagram, and {0002} and $\{10\bar{1}0\}$ pole figure, shows the EBSD results of the pre-deformed samples under different

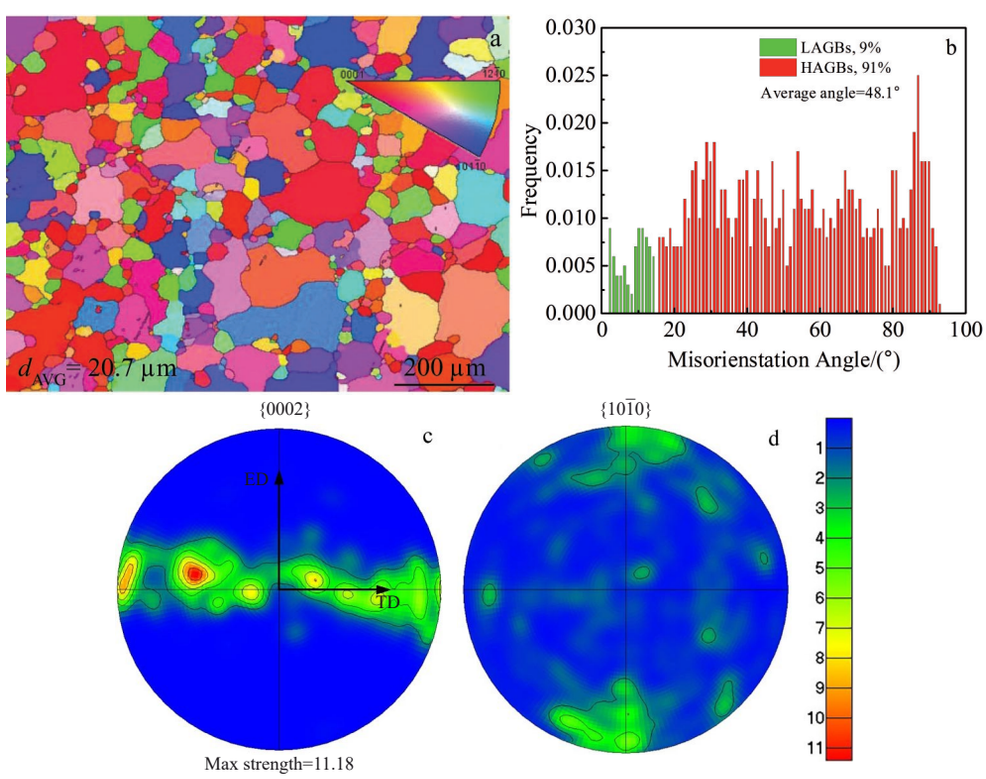

Fig.5 Initial microstructure characteristics of as extruded AZ31 magnesium alloy: (a) IPF diagram, (b) grain boundary misorientation, (c) {0002} pole figure, and (d) $\{10\bar{1}0\}$ pole figure

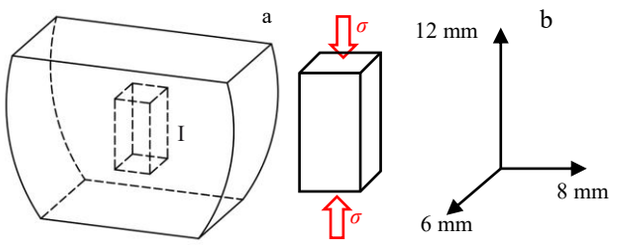

Fig.6 Sampling method of secondary compression sample: (a) sampling position and (b) the secondary compression sample

strain paths. The red line represents the $\{10\bar{1}2\}$ tension twin. The blue line represents the $\{10\bar{1}1\}$ compression twin. The purple line represents the $\{10\bar{1}1\}$-$\{10\bar{1}2\}$ double twin. The volume fraction of the twins is shown in Table 1. As shown in Fig. 7a, a large number of $\{10\bar{1}2\}$ tension twin lamellae are formed in the //ED-3% grains of the pre-deformed sample, and the content is approximately 30.9% (Table 1). This configuration indicates that the deformation is dominated by twinning in the pre-deformed stage. The average grain size is 10.9 μm due to the subdivision of twin boundary grains[17]. When the sample is compressed along the ED direction, it is in the compression loading state and positioned perpendicular to the *c*-axis. A low CRSS of the matrix means that the condition is favorable for the formation of $\{10\bar{1}2\}$ tension twins and can adapt to the compressive strain[18]. The $\{10\bar{1}2\}$ tension twin causes the *c*-axis of the grain oriented on the base plane to turn by approximately 86°[19]. This condition weakens the {0002} strong basal texture. The *c*-axis is perpendicular to the ED direction, whereas the formation of the *c*-axis twin texture is parallel to the ED direction. In addition, the polar density of the $\{10\bar{1}0\}$ prismatic texture gradually shifts to the TD direction, as shown in Fig. 2. The number of $\{10\bar{1}2\}$ tension twins in ⊥ED-3%, with an average grain size of 13.2 μm, is much less (7.19%) than that in //ED-3%. When the pre-deformation direction is ⊥ED, the formation of the $\{10\bar{1}2\}$ tension twins becomes less apparent, and a slip dominates the plastic deformation. However, in the process of pre-deformation, twinning also exhibits part of the regulating effect on deformation. The {0002} strong basal texture gradually transforms into a twin texture whose *c*-axis is parallel to the TD. As shown in Fig. 7, $\{10\bar{1}1\}$ compression twins and $\{10\bar{1}1\}$-$\{10\bar{1}2\}$ double twins can be slightly observed, which may be attributed to the effect of pre-deformation.

Fig. 8 shows the Kernel Average Misorientation (KAM) of the pre-deformed samples under different strain paths. The KAM diagram can be used to illustrate the dislocation density and strain degree of microstructure[20,21]. Although only geometrically necessary dislocations need to be considered when evaluating stored energy, KAM can also offer a good indication of regions with high storage strain and dislocation

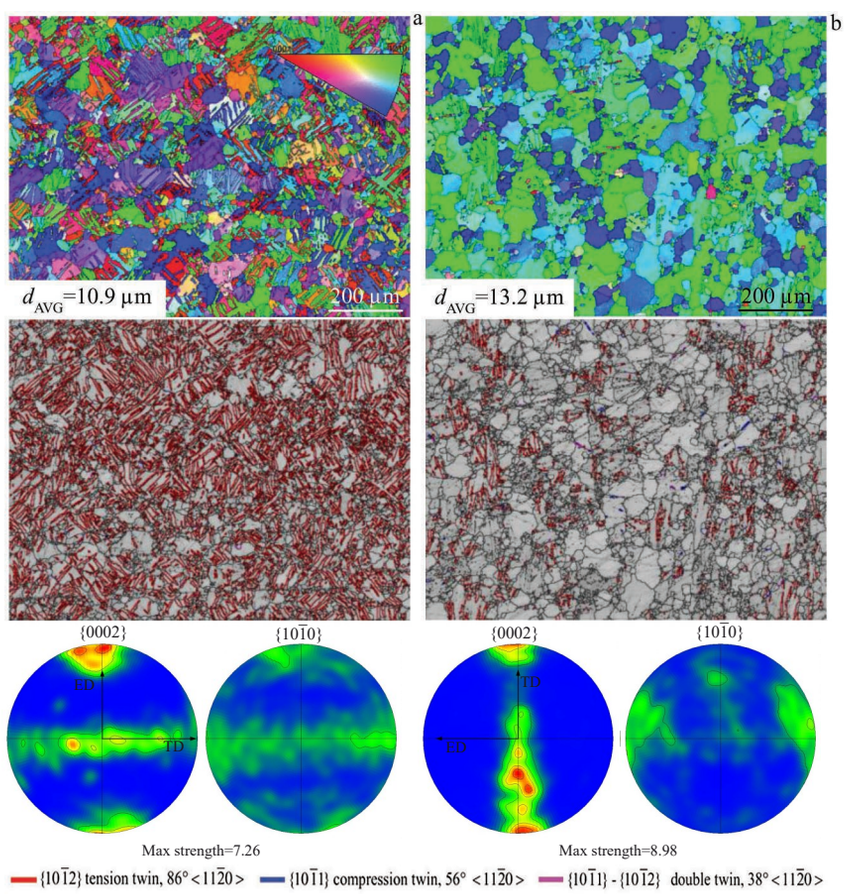

Fig.7 Microstructures and pole figures of pre-deformed samples: (a) //ED-3% and (b) ⊥ED-3%

Table 1 Volume fraction of twins in pre-deformed samples (vol%)

Twin type	//ED-3%	⊥ED-3%
$\{10\bar{1}2\}$	30.90	7.19
$\{10\bar{1}1\}$	0.08	0.30
$\{10\bar{1}1\}$-$\{10\bar{1}2\}$	0.03	0.14

density[22]. The green and red areas in the figure represent high KAM values, while the blue area represents low KAM values. As shown in Fig.8a, a large number of twin bands form in the //ED-3% grains of the pre-deformed sample. The strain is concentrated near the twin boundary, which acts as an obstacle to the dislocation slip, resulting in a significant increase in dislocation density[23]. Meanwhile, in ⊥ED-3%, the dislocation

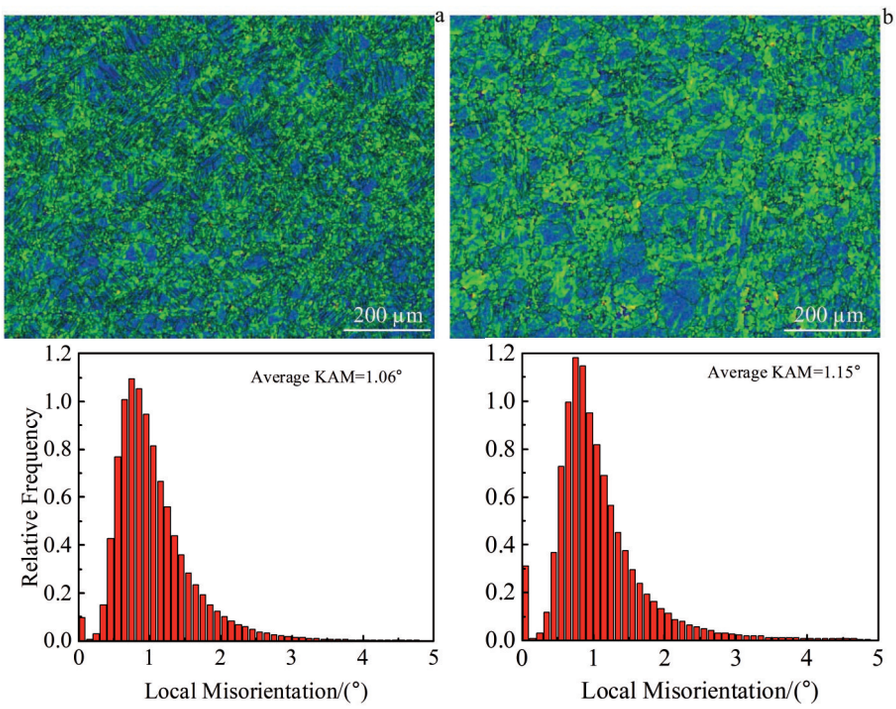

Fig.8 KAM diagrams of pre-deformed samples: (a) //ED-3% and (b) ⊥ED-3%

walls are distributed in most of the grains. Only a few parts of the larger grains have relatively small dislocations and strains, and the storage strain energy is low. The average KAM values of pre-deformed //ED-3% and ⊥ED-3% samples are 1.06° and 1.15°, respectively.

2.2 Secondary compression experiment

Fig. 9 shows the stress-strain curves of the pre-deformed samples under secondary compression in which the anisotropy is obvious. Its relative compression performance is shown in Table 2. The //ED-0% sample without pre-deformation has a low yield strength of 87 MPa and compressive strength of 300 MPa. However, the stress-strain curve changes after 3% of pre-deformation, and the curve is in the shape of "S". The yield strength is 145 MPa, and the ultimate strength is 400 MPa. The mechanical properties of the samples in the two states are subsequently compared. Given the high-density twin layer and the dislocation hardening, the twinning after the pre-deformation has induced a refinement hardening based on the density of the twin lamellae[24]. The twin boundary hinders the dislocation movement, illustrative of the Hall-Petch effect[25], causing the yield strength and ultimate strength to increase significantly during the secondary compression. For the ⊥ED-3% sample, the refinement and hardening are weak due to the low density of the twin layer. The increase in yield strength is a result of the dislocation hardening. The yield strength of //ED-3% and ⊥ED-3% is increased by 66.7% and 66% compared to that of //ED-0% and ⊥ED-0%, respectively.

Fig. 10 shows the relationship between the work hardening rate θ and net strain ($\varepsilon - \varepsilon_{0.02}$) of the pre-deformed samples during secondary compression. The initial work hardening rate of the //ED-3% and ⊥ED-3% of the pre-deformed samples is increased, and the work hardening rate is gradually

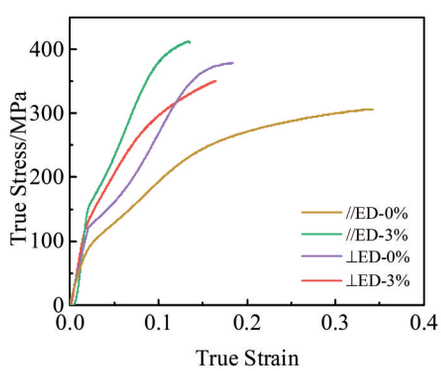

Fig.9 Stress-strain curves of the pre-deformed samples under secondary compression

Table 2 Mechanical properties of pre-deformed samples under secondary compression

Sample	Yield strength/MPa	Ultimate strength/MPa
//ED-0%	87	300
//ED-3%	145	400
⊥ED-0%	121	378
⊥ED-3%	129	350

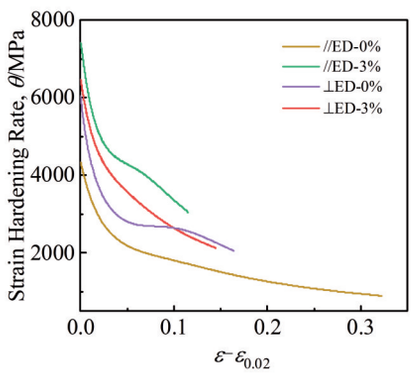

Fig.10 Strain hardening rate curves of pre-deformed samples during secondary compression

decreased with the increase in strain. Previous studies have shown that the strain hardening rate curve can be divided into three stages as follows. In stage I, the strain hardening rate decreases with the appearance of the basal slip and tension twins. In stage II, the slip, twinning, and slip interaction and the formation of a double twinning promote strain hardening, but the formation of $\{10\bar{1}2\}$ tension twinning causes the grain orientation to change to the "hard" direction. The strain hardening rate of the textural strengthening is also increased. In stage III, the strain hardening rate reaches the peak value upon completion of the twinning in the twin saturation region. At the same time, the ability of the twins to block the dislocation movement is reduced because of stress concentration, further leading to the dislocation locking at the twin interface and the decrease in strain hardening rate [26-28].

As shown by the ⊥ED-0% sample in Fig. 10, with the further increase in the strain, the deformation speed of the sample slows down, and a platform appears in stage II (strain of 5%~10%). Although //ED-3% has no obvious plateau in stage II, the curve undergoes two slope changes. The twin intersection and dislocation accumulation at the twin boundary are longer for ⊥ED-0% (or //ED-3%) sample compared with those of ⊥ED-3% (or //ED-0%) sample. The flow stress accumulates in the sample, and the strain hardening increases significantly, resulting in a corresponding increase in ultimate strength. This trend is consistent with the finding of Wang et al[29]. The work hardening in stage II does not appear in //ED-0% and ⊥ED-3%, and the strain hardening rate gradually decreases with the increase in strain until the sample is broken.

Fig. 11, which includes the IPF diagram, grain boundary structure diagram, {0002} and $\{10\bar{1}0\}$ pole figure, shows the EBSD results of the pre-deformed samples after 8% of secondary compression. Fig. 12 shows the KAM diagram of pre-deformed samples after secondary compression to 8%.

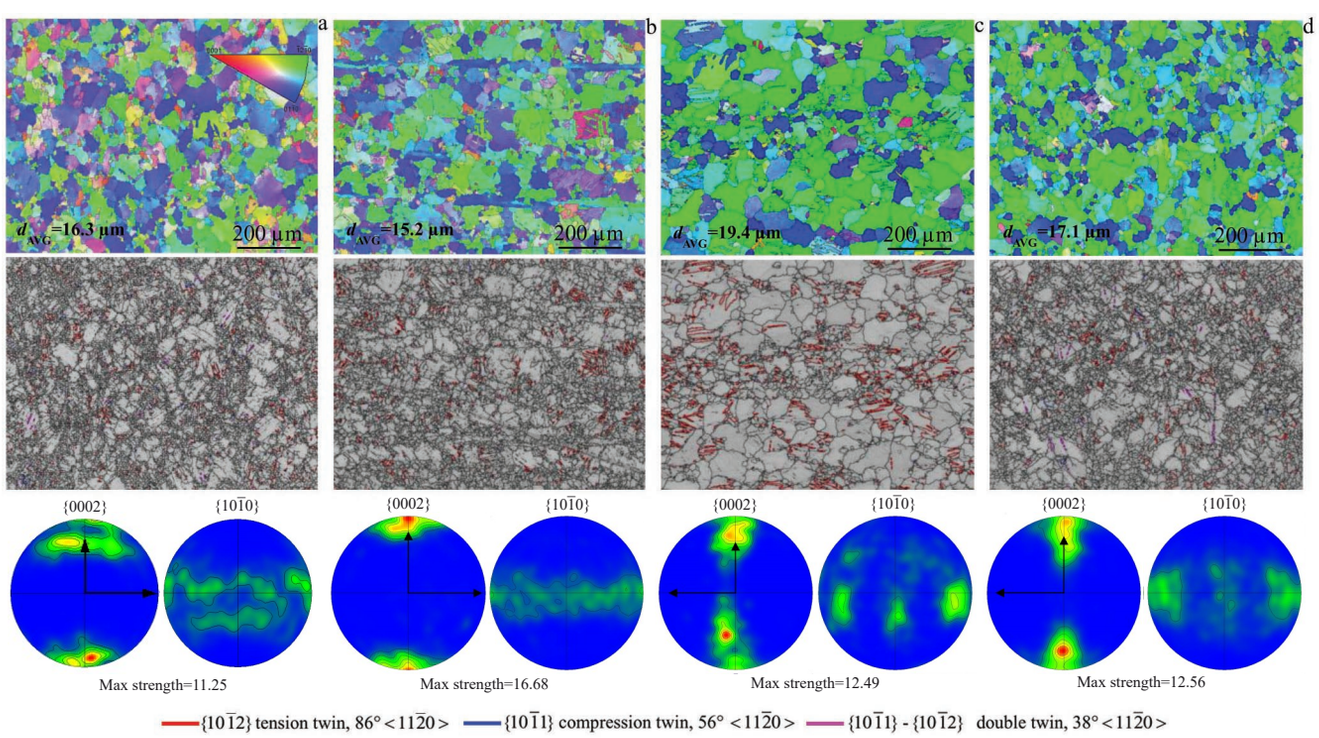

Fig.11 Microstructures and pole figures of the pre-deformed samples after secondary compression to 8%: (a)//ED-0%, (b)//ED-3%, (c) ⊥ED-0%, and (d) ⊥ED-3%

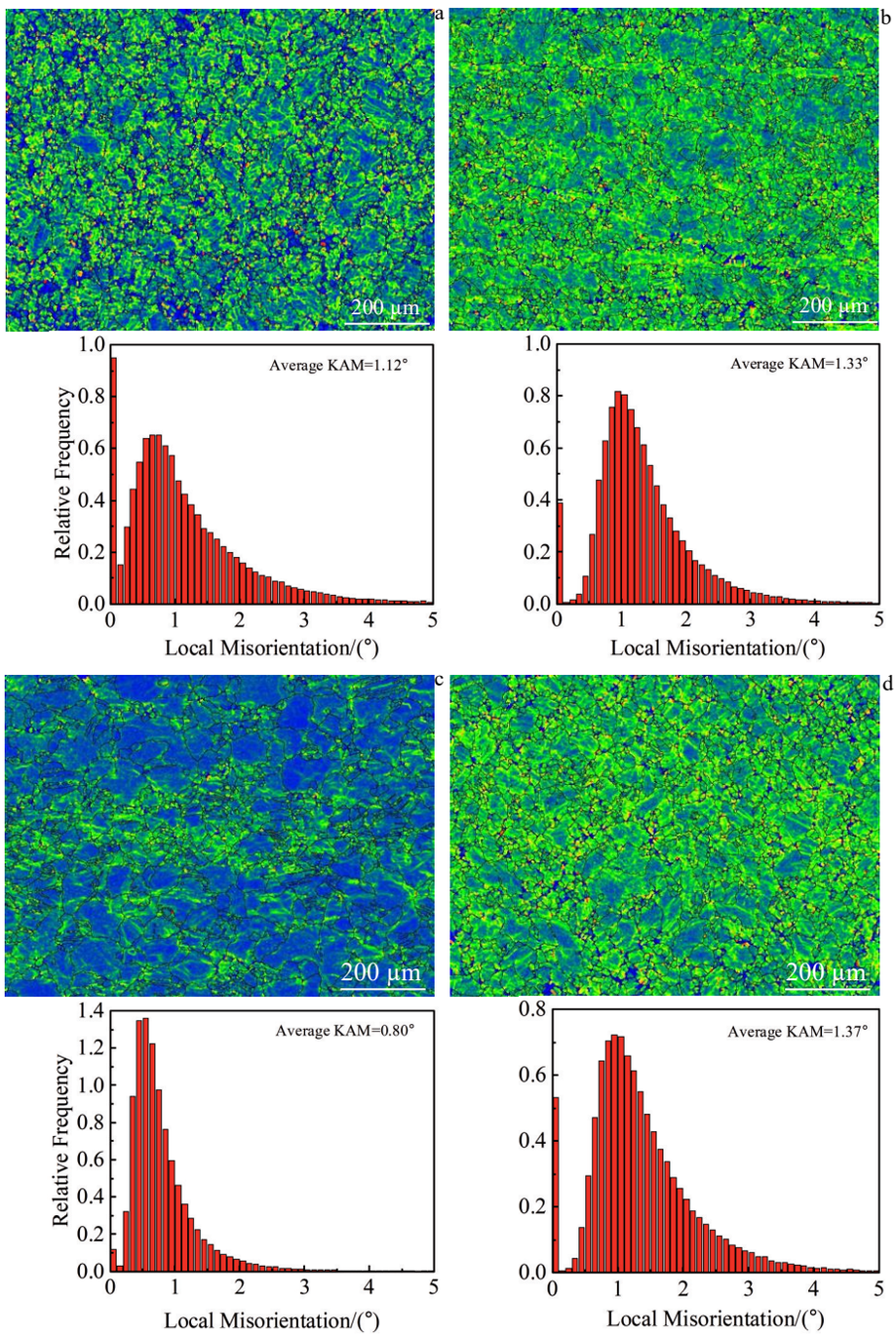

Fig.12 KAM diagrams of pre-deformed samples after secondary compression to 8%: (a)//ED-0%, (b)//ED-3%, (c) ⊥ED-0%, and (d) ⊥ED-3%

Table 3 Twin volume fraction of pre-deformed samples after secondary compression to 8% (vol%)

Twin type	//ED-0%	//ED-3%	⊥ED-0%	⊥ED-3%
$\{10\bar{1}2\}$	2.47	3.00	11.50	2.11
$\{10\bar{1}1\}$	0.18	0.02	0.07	0.12
$\{10\bar{1}1\}$-$\{10\bar{1}2\}$	0.34	0.06	0.05	0.31

The volume fraction of the twins is shown in Table 3. The average grain size of //ED-3% (or ⊥ED-3%) is smaller than that of //ED-0% (or ⊥ED-0%), and the volume fraction of the $\{10\bar{1}2\}$ tension twins is lower than that of the pre-deformed samples. The decrease in twin boundary with the increase in strain can be explained by the growth and combination of the tension twins during secondary compression[30]. The corresponding decrease of the $\{10\bar{1}1\}$ compression twins and the increase of the $\{10\bar{1}1\}$-$\{10\bar{1}2\}$ double twins become apparent (Table 3). At the same time, as the pre-deformed samples is in stage II of machining hardening when the secondary compression reaches 8%, the twin volume fraction

also indicates that the accumulation of flow stress of ⊥ED-0% (or ∥ED-3%) is higher than that of ⊥ED-3% (or ∥ED-0%). Compared with the initial texture shown in Fig. 5 and Fig. 7a, the {0002} strong basal texture of the ∥ED-0% and ∥ED-3% samples whose *c*-axis is perpendicular to the ED direction disappears, and a twin texture whose *c*-axis is approximately parallel to the ED direction is formed. The textural strength of ∥ED-3% is greater than that of ∥ED-0%. The findings suggest that the enhancement of the twin texture may play an important role in the secondary compression process. Similarly, ⊥ED-3% has a texture whose *c*-axis is approximately parallel to the TD. Compared with the findings for ⊥ED-0%, the {0002} basal textural strength of ⊥ED-3% is almost unchanged, indicating that the plastic deformation process in the ⊥ED direction is mainly dominated by a slip. These twin textural characteristics are consistent with the results of the $\{10\bar{1}2\}$ twin texture of other magnesium alloys[31,32].

As seen in Fig. 12, almost all grains of the ∥ED-0% sample have a high dislocation density and strain after the single-pass compression, and the average KAM value is 1.12°. Given the high dislocation density and high strain in the pre-deformed sample (Fig. 8a), the interaction between dislocation and twin boundary will be enhanced during the secondary compression, which is helpful in increasing the pinning effect of the twin boundary movement[33]. Moreover, as the change in orientation is drastic, the position of the grain boundary cannot be easily distinguished. The dislocation walls are densely distributed and intertwined. The average KAM value for this configuration is 1.33°. Similarly, as shown in Fig. 12c and 12d, the ⊥ED-0% sample without pre-deformation mainly produces dislocation walls near the grain boundaries, but the distribution of dislocation walls in the grains is relatively sparse (average KAM value of 0.80°). After the pre-deformation, a strain concentration appears in the grain during secondary compression, and the strain concentration at the grain boundary increases gradually (average KAM value of 1.37°). The above analysis further indicates that the generation and accumulation of the dislocations are enhanced during secondary compression due to the change in the strain path. At the same time, the growth of tension twins is hindered by the dislocations, and the interaction between dislocations and twin boundaries is strengthened, resulting in a small increase in the $\{10\bar{1}1\}$-$\{10\bar{1}2\}$ double twins (Table 3).

3 Conclusions

1) More dislocations and strains are produced during secondary compression of AZ31 magnesium alloy because of the pre-deformation. Moreover, with the initiation of the $\{10\bar{1}2\}$ tension twins during pre-deformation, a large amount of strain energy is accumulated in the sample. The interaction between the dislocation and the twin boundary is enhanced during the secondary compression, resulting in the increase in dislocation density.

2) Pre-deformation direction is of great significance in improving the yield strength of the secondary compression. The yield strength of ∥ED-3% and ⊥ED-3% is increased by 66.7% and 6.6% compared to that of ∥ED-0% and ⊥ED-0%, respectively.

3) When the pre-deformation direction is ∥ED (or ⊥ED), the {0002} basal texture disappears gradually, and the twin texture whose *c*-axis is parallel to the ED (or TD) increases gradually. With 8% of secondary compression, the twin texture completely changes to the direction of *c*-axis, making it parallel to the ED (or TD).

4) Both the increase in grain refinement and dislocation density are the main reasons for the increase in the yield strength of the secondary compression. However, for ∥ED-3%, the weakening of the basal texture (or the strengthening of the twin texture) may play an important role in improving the mechanical properties of the AZ31 magnesium alloy.

References

1 Hou Dewen, Liu Tianmo, Chen Huicong *et al. Materials Science and Engineering A*[J], 2016, 660: 102

2 Zhang Lei, Liu Chunguo, Wang Huiyuan *et al. Materials Science and Engineering A*[J], 2014, 597: 376

3 Mustafa Kemal Kulekci. *The International Journal of Advanced Manufacturing Technology*[J], 2008, 39(9-10): 851

4 Liu Pei, Xin Yunchang, Liu Qing *et al. Transactions of Nonferrous Metals Society of China*[J], 2011, 21(4): 880

5 Chu Zhibing, Zhang Duo, Ma Lifeng *et al. Rare Metal Materials and Engineering*[J], 2018, 47(1): 124

6 Zhu S Q, Ringer S P. *Acta Materialia*[J], 2018, 144: 365

7 Wang Fulin, Agnew Sean R. *International Journal of Plasticity* [J], 2016, 81: 63

8 Al-Samman T, Gottstein G. *Materials Science and Engineering A* [J], 2008, 488(1-2): 406

9 Park Sung Hyuk, Lee Jeong Hun, Moon Byoung Gi *et al. Journal of Alloys and Compounds*[J], 2014, 617: 277

10 Wang Bingshu, Deng Liping, Guo Ning *et al. Materials Characterization*[J], 2014, 98:180

11 Su Hui, Chu Zhibing, Xue Chun *et al. Materials Research Express*[J], 2020, 7(8): 86 503

12 Hou Dewen, Liu Tianmo, Luo Longjing *et al. Materials Characterization*[J], 2017, 124: 122

13 Song Bo, Xin Renlong, Chen Gang *et al. Scripta Materialia*[J], 2012, 66(12): 1061

14 Wang Haixuan, Chen Wenzhen, Zhang Wencong *et al. Materials Science and Engineering A*[J], 2021, 806: 140 807

15 Márquez E V, Mocellin K, Toualbi L *et al. Journal of Nuclear Materials*[J], 2012, 420(1-3): 479

16 Montmitonnet P, Logé R, Hamery M *et al. Journal of Materials Processing Technology*[J], 2002, 125-126: 814

17 Song Guangsheng, Jiang Jingqian, Chen Shuaifeng *et al. Rare Metal Materials and Engineering*[J], 2017, 46(11): 3512 (in Chinese)

18 Chino Yasumasa, Kimura Katsuya, Hakamada Masataka *et al.*

Materials Science and Engineering A[J], 2008, 485(1-2): 311
19 Proust Gwénaëlle, Tomé Carlos N, Jain Ashutosh *et al. International Journal of Plasticity*[J], 2009, 25(5): 861
20 Li Jin, Jie Dong, Jie Sun *et al. International Journal of Plasticity* [J], 2015, 72: 218
21 Yang Yi, Yang Xuyue, Xiao Zhenyu *et al. Materials Science and Engineering A*[J], 2017, 688: 280
22 Victoria-Hernández J, Suh J, Yi S *et al. Materials Characterization*[J], 2016, 113: 98
23 Salem A A, Kalidindi S R, Semiatin S L. *Acta Materialia*[J], 2005, 53(12): 3495
24 Xin Yunchang, Wang Maoyin, Zeng Zhen *et al. Scripta Materialia*[J], 2012, 66(1): 25
25 Yu Huihui, Xin Yunchang, Wang Maoyin *et al. Journal of Materials Science & Technology*[J], 2018, 34(2): 248
26 Asgari H, Szpunar J A, Odeshi A G *et al. Materials Science and Engineering A*[J], 2015, 633: 92
27 Jiang Lan, John J Jonas, Alan A Luo *et al. Materials Science and Engineering A*[J], 2007, 445-446: 302
28 Korla Rajesh, Chokshi Atul H. *Scripta Materialia*[J], 2010, 63(9): 913
29 Wang Zhi, Cao Gengsheng, Wang Feng *et al. Materials Characterization*[J], 2021, 172: 110 839
30 Mokdad F, Chen D L, Li D Y. *Materials & Design*[J], 2017, 119: 376
31 Lee Jeong Hun, Park Sung Hyuk, Hong Seong Gu *et al. Scripta Materialia*[J], 2015, 99: 21
32 Kim Ye Jin, Lee Jong Un, Kim Young Min *et al. Journal of Magnesium and Alloys*[J], 2020, 46(11): 3512
33 Xin Yunchang, Lv Liangchen, Chen Houwen, *et al. Materials Science and Engineering A*[J], 2016, 662: 95

应变路径变化对AZ31镁合金力学行为的影响

李鱼鱼[1]，韩廷状[2]，楚志兵[1]，薛　春[1]，杨千华[1]，赵晓东[1]，高　虹[3]
(1. 太原科技大学 材料科学与工程学院，山西 太原 030024)
(2. 西北工业大学 材料科学与工程学院，陕西 西安 710072)
(3. 江苏武进不锈股份有限公司，江苏 常州 213000)

摘　要：以挤压态AZ31镁合金棒材为原材料，在室温下沿着//ED和⊥ED的方向进行预变形实验，模拟二辊皮尔格冷轧过程中减壁段横截面瞬时变形应力状态，接着对预变形试样取样进行二次压缩，利用电子背散射衍射（EBSD）对2次变形之后的微观结构进行表征。研究了应变路径变化情况下组织和织构对力学行为的影响。结果表明，预变形使AZ31镁合金的屈服强度提高，其主要原因是预变形产生的{10$\bar{1}$2}拉伸孪晶导致晶粒细化和位错密度增加。并且孪晶的出现会改变晶粒的取向，基面织构弱化（或孪生织构增强）在改善AZ31镁合金力学性能方面可能起到更重要的作用。//ED-3%和⊥ED-3%试样的屈服强度分别提高了66.7%和6.6%。

关键词：AZ31镁合金；应变路径；力学行为；孪晶；位错；织构

作者简介：李鱼鱼，男，1995年生，硕士，太原科技大学材料科学与工程学院，山西 太原 030024，E-mail：905409420@qq.com